Supporting Information

Increasing the sensitivity of electrochemical DNA detection by a micropillar-structured biosensing surface

Jacopo Movilli[†,a] *Ruben W. Kolkman*[†,a,b] *Andrea Rozzi,*[c] *Roberto Corradini,*[c] *Loes I. Segerink,*[b] *Jurriaan Huskens*[a,*]

[a] Molecular Nanofabrication Group, MESA+ Institute for Nanotechnology, Department of Science and Technology, University of Twente, P.O. Box 217, 7500 AE, Enschede, The Netherlands

[b] BIOS Lab on a Chip group, MESA+ Institute for Nanotechnology, Technical Medical Centre, Max Planck Institute for Complex Fluid Dynamics, University of Twente, The Netherlands

[c] Department of Chemistry, Life Sciences and Environmental Sustainability, University of Parma, Parco Area delle Scienze 17/A, 43124 Parma, Italy

[†] Equal first author contributions

*Corresponding author: j.huskens@utwente.nl

Supporting Figures

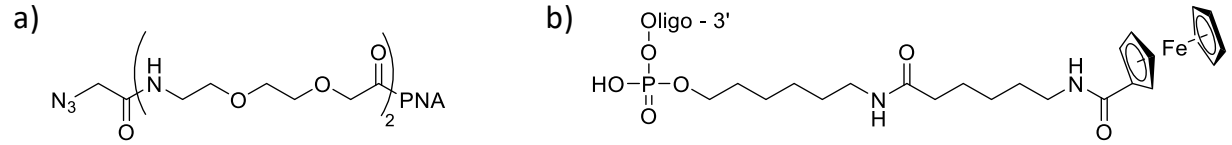

Figure S1. Chemical structures of a) PNA and b) DNA linkers to respectively anchor azide and ferrocene moieties. The [2-(2-aminoethoxy)ethoxy]acetyl (AEEA) PNA linker, with 2-azidoacetyl functional group, was already reported in a previous work.[1] A new batch of this PNA was produced and characterized (see Figure S2 and S3 for batch characterization).

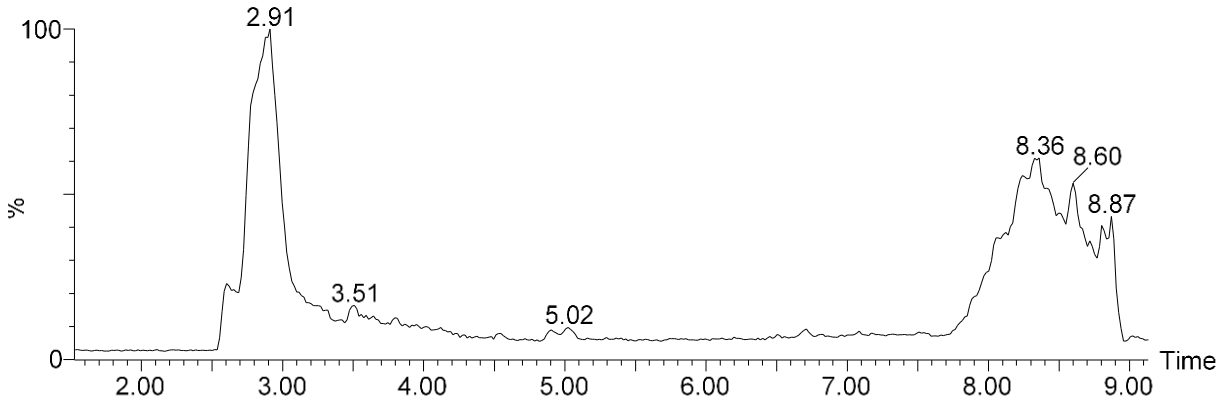

Figure S2. Chromatogram of probe the batch of PNA-N_3, used for the present work; peak at 2.91 min corresponds to the target PNA. For comparison of other batches, see ref. 1.

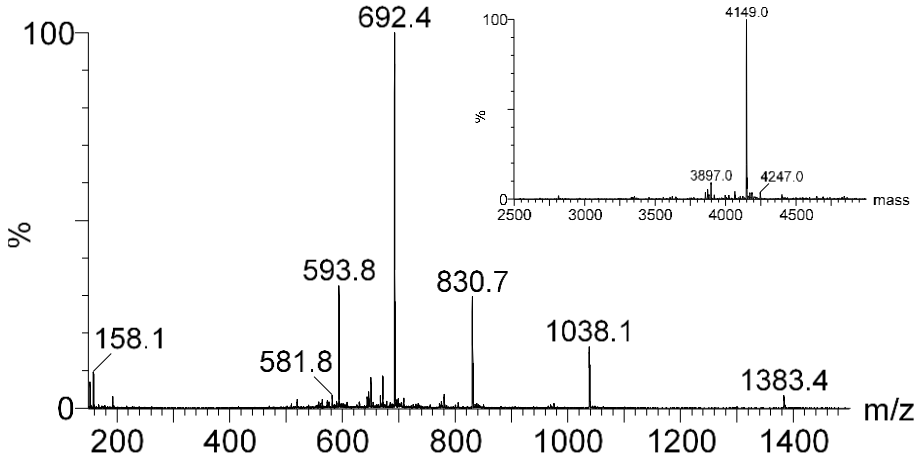

Figure S3. Mass spectrum of PNA-N_3, multicharged ions: 1384 $[MH_3]^{3+}$, 1038 $[MH_4]^{4+}$ 831 $[MH_5]^{5+}$, 692 $[MH_6]^{6+}$, 594 $[MH_7]^{7+}$. The inset shows the reconstructed molecular mass: calculated MW 4147.1, *m/z found* 4149.0.

Table S1. Sequences of DNA and PNA molecules used in this work

Oligo	Sequence 5'→ 3'(number of nucleotides)	Role
PNA-N_3	N_3-CTA CGC CAC CAG CT-Gly-NH_2 (14); ε (260 nm): 127900 $M^{-1}cm^{-1}$	PNA probe WT KRAS
cDNA	ATG ACT GAA TAT AAA CTT GTG GTA GTT GGA GCT GGT GGC GTA G (43)	Target, complementary to PNA-N_3
ncDNA	CTA CGC CAC CTC AAC CTA CGC CAC CTC CAC CTA CGC CAC CTC (42)	Non complementary to PNA-N_3
rDNA-Fc	ACC ACA AGT TTA TAT TCA GTC AT-Fc (23)	Reporter, complementary to the 5'end of cDNA

PNA-N_3 was chosen with a sequence that have been shown to be a relevant tract of the KRAS gene subject to point mutations present in several tumors.[2,3]

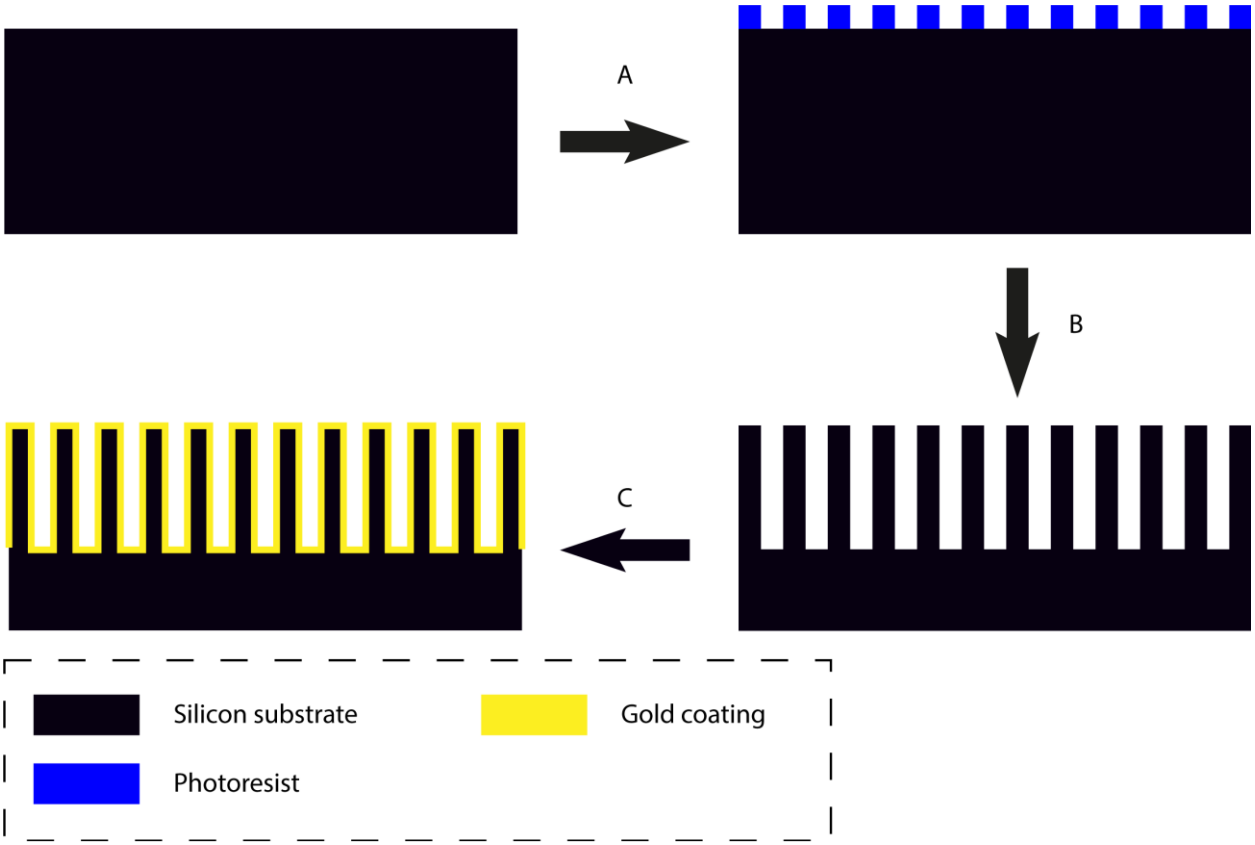

Figure S4. Schematic illustration of the fabrication process of micropillar-structured substrates. (A) Deposition of photoresist on silicon wafer followed by patterning of the photoresist by photolithography. (B) Deep reactive ion etching to create the micropillar-structured substrate. (C) Coating of the micropillar-structured substrate with gold by sputtering.

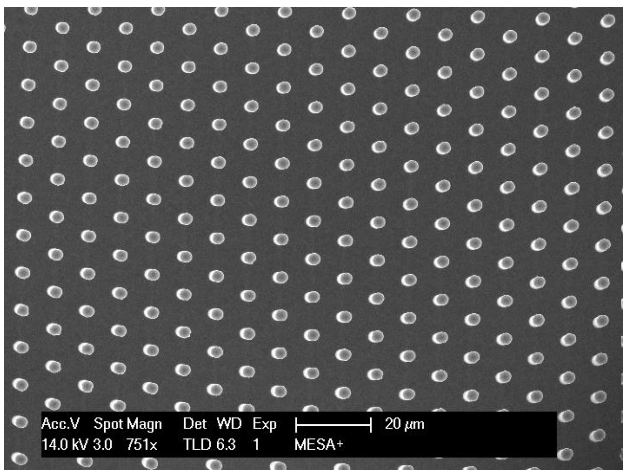

Figure S5. Top-view SEM image of a micropillar array (10 µm pitch), showing the hexagonal design of the micropillar section.

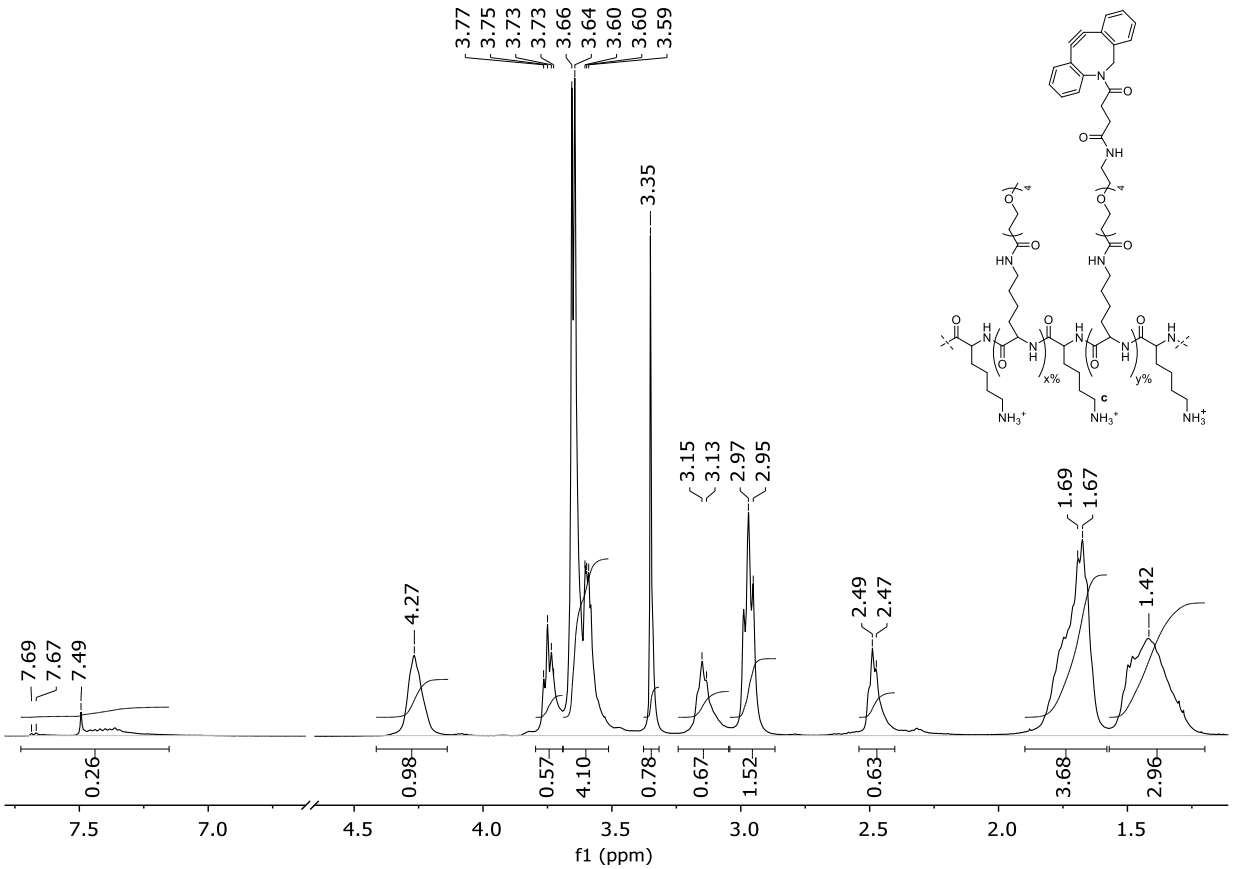

Figure S6. ^{1}H-NMR spectra of PLL-OEG-DBCO after purification by dialysis. Quantification of the grafted OEG and DBCO percentages, 27.6% and 3.0%, respectively, has been performed according to a previously published procedure (see below).[4,5]

PLL-OEG(27.6%)-DBCO(3%)

Quantification of OEG and DBCO grafted densities were obtained according to our previously reported procedure,[4,5] using the integral ratios of the characteristic signals in the ^{1}H-NMR spectra (see Figure S6). Integrals were normalized to the peak at 4.27 ppm (lysine backbone), and the ones at 2.96 ppm (free lysine), 3.14 ppm (functionalized lysine of both DBCO and OEG side groups, and 7.22-7.69 ppm (DBCO) were used for the calculations.

All the integrals used correspond to two protons, except the DBCO one, which corresponds to eight. Consequently, it was normalized by dividing for a factor of four. The sum of the integrals

of free and functionalized lysine correspond to the total amount of lysine at the PLL backbone. Therefore:

$$PLL\ functionalization\ (\%) = \frac{integral\ of\ functional\ Lys}{integrals\ of\ free\ Lys + functional\ Lys} \quad \text{eq. 1}$$

$$DBCO\ functionalization\ (\%) = \frac{(DBCO\ integral)/4}{integrals\ of\ free\ Lys + functional\ Lys} \quad \text{eq. 2}$$

$$OEG\ functionalization\ (\%) = PLL\ functionalization - DBCO\ functionalization \quad \text{eq. 3}$$

Table S2. Water contact angle values of gold-coated flat (∞ pitch) and micropillar-structured Si substrates (19 µm and 8 µm pitch) before and after UV-ozone activation, and after immersion in a 1 mg/ml PLL-OEG-DBCO solution in PBS at pH 7.4 (control substrates in PBS without PLL). Next, the substrates were immersed in PBS (pH 7.4) for 24 h and the contact angle values monitored again. Standard deviations (in brackets) were calculated measuring three different spots of the same substrate.

Pitch size (µm)	Before activation	After activation	After 1 h of PLL-OEG-DBCO	After 24 h in PBS 7.4
Flat	59.9° (±1.3°)	<15°	31.6° (±1.5°)	32.7° (±1.9°)
Flat (control)	/	<15°	<20° (only PBS)	38.6° (±2.2°)
19	96.2 (±2.3°)	<15°	34.4° (±2.8°)	36.1° (±3.2°)
19 (control)	/	<15°	<20° (only PBS)	45.2 (±4.1°)
8	104.3 (±1.8°)	<15°	35.9° (±2.0°)	37.4° (±2.3°)
8 (control)	/	<15°	<20° (only PBS)	46.2 (±2.6°)

Electrochemical analysis

Active surface area determination

The projected areas of the total (PA_{tot}, 0.44 cm^2), flat (PA_f, 0.19 cm^2) and pillared (PA_p, 0.25 cm^2) sections for electrochemical substrates are shown in Figure 4. Assuming absence of surface imperfections, the total geometric surface area (A_{tot}), is given by eq. 4:

$$A_{tot} = A_f + A_p \qquad \text{eq.4}$$

Where A_f and A_p are the geometric areas of the flat and pillared sections of a micropillar-structured substrate, respectively. In particular, for the flat section:

$$A_f = PA_f \qquad \text{eq.5}$$

while for the pillared section:

$$A_p = PA_p\left(1 + \frac{2}{3}\sqrt{3} \cdot \pi \frac{d_p \cdot h_p}{p^2}\right) \qquad \text{eq. 6}$$

where d_p is the pillar diameter (4 μm), h_p the pillar height (36.7 μm), and p the pitch (μm). The factor $1+\frac{2}{3}\sqrt{3} \cdot \pi \cdot d_p \cdot h_p/p^2$ is the factor SE_p by which the surface area of a unit cell containing a single pillar in a hexagonal design increases from flat to pillar (see Figure S7). Without a micropillar in this unit cell, the area is $\frac{1}{2}\sqrt{3} \cdot p^2$. When a micropillar is placed in the unit cell, the area is increased with the sides of the pillar, amounting to $\pi \cdot d_p \cdot h_p$, leading to a total area of $\frac{1}{2}\sqrt{3} \cdot p^2 + \pi \cdot d_p \cdot h_p$. Taking the ratio between these areas leads to the aforementioned surface enhancement factor in the pillar area, SE_p.

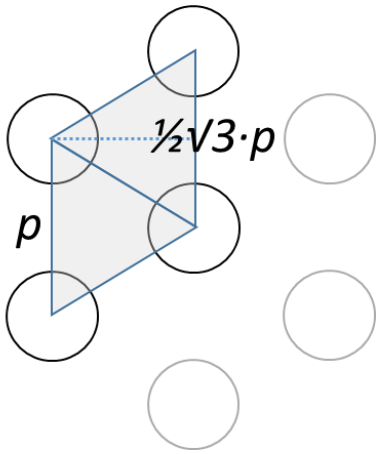

Figure S7. Section of the hexagonal micropillar array with the two triangles jointly covering one micropillar.

For simplicity, we ignored effects of the non-perfect fit of the hexagonal pillar lattice in the square pillar area (error on the total number of pillars is <0.002 %), and the sidewall surrounding the pillar section, introduced by etching the pillars into the substrate (estimated to be < 1%). Therefore, the total theoretical surface enhancement factor (SE_{tot}) by the incorporation of micropillars is given by A_{tot}/PA_{tot}.

Contributions from roughness factors (sputtered gold and DRIE etching process) can be responsible for the differences in values between the calculated geometric and experimentally (CV) determined surface areas. Therefore, two roughness factors were defined, one for the flat area (s_f = 1.29), ascribed to the sputtering of gold, and one for the pillared section (s_p = 1.48), attributed to the DRIE etching process and the gold sputtering. In detail, s_f was calculated by the ratio between the experimentally determined surface area ($A_{tot,exp}$ = 0.57 cm^2) and the geometric surface area (A_{tot} = 0.44 cm^2) of a flat gold surface, while s_p was calculated from the slope of the linear fit from the relationship between the experimental determined surface areas and the geometrical ones for the pillared section using various pitch sizes. For this linear fit, the experimentally (CV) determined areas for the pillared section (Figure S8), obtained by subtracting

the flat area (by taking the corresponding fraction of the experimental surface area of the flat sample) from the total area, were plotted versus the geometric area of the same pillared part (A_p) as shown in Figure S9. The calculated geometric surface areas including both roughness factors, were then calculated by multiplying the terms A_f and A_p respectively with s_f and s_p. Consequently, the calculated surface enhancement factors, relative to the experimental flat area, were determined.

Table S3. Geometrical areas and theoretical surface enhancement factors for the total area (A_{tot} and SE) and pillared section (A_p and SE_p) without surface roughness using eqs. 4-6.

Pitch size (µm)	A_{tot}	A_p	SE	SE_p
Flat ($p = \infty$)	0.44	0.25	1	1
19	0.81	0.62	1.83	2.48
8	2.52	2.33	5.71	9.32

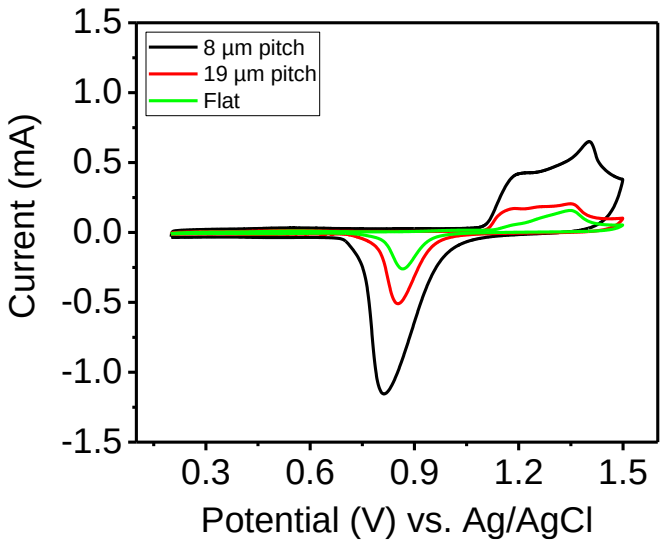

Figure S8. Cyclic voltammograms of gold-coated p^{++} type silicon micropillar-structured substrates with pitch 8 µm and 19 µm (black and red lines, respectively) and flat one (green line). Experiments were performed in 0.1 M H_2SO_4 with a scan rate of 100 mV/s.

Table S4. Experimental areas for flat and micropillar-structured (19 and 8 µm pitch) electrodes using 0.1 M H_2SO_4 solution at CV experiments with a scan rate of 100 mV/s

Pitch size (µm)	$A_{tot,exp}$ (cm^2)
Flat ($p = \infty$)	0.57
19	1.26
8	3.68

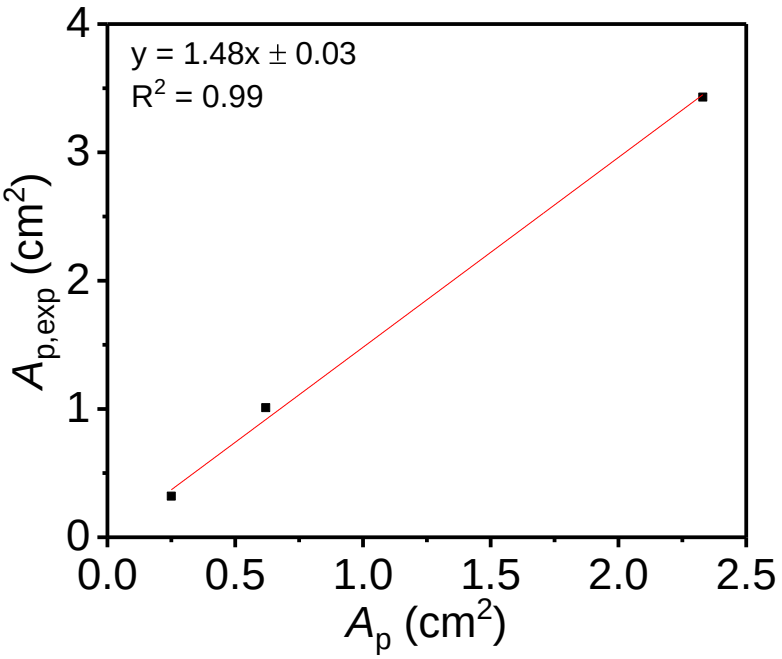

Figure S9. Experimental (CV in 0.1 M aq. H_2SO_4)[6] surface area of the pillar section ($A_{p,exp}$) of flat and micropillar-structured substrates as a function of the geometric surface area of the pillar section without surface roughness (A_p). The surface roughness factor in the pillared section (s_p = 1.48) was determined from the slope of a linear fit through the origin.

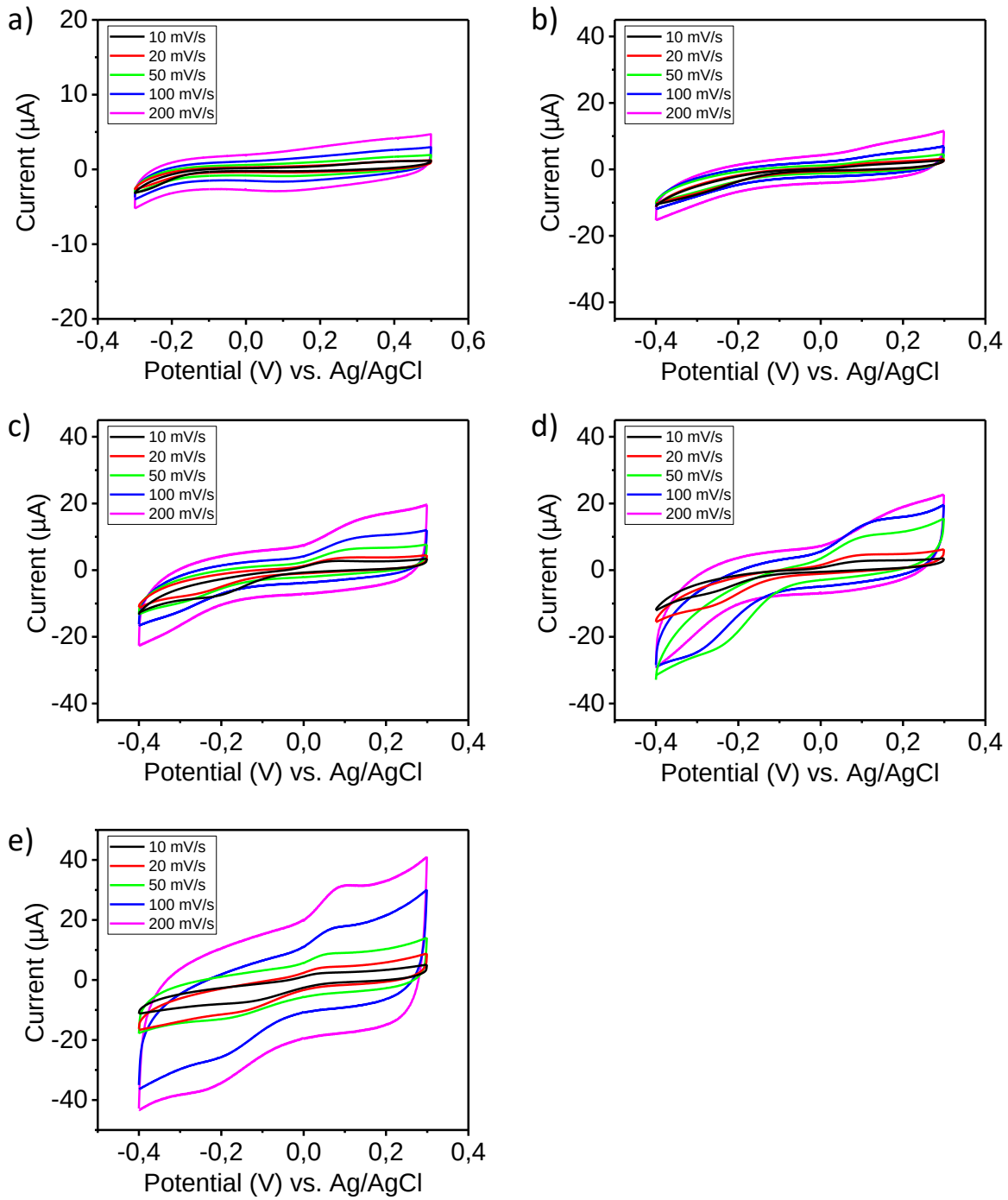

Figure S10. Cyclic voltammograms of PLL-OEG(27.6)-DBCO(3.0)-functionalized Au coated substrates after anchoring of PNA-N_3 and the consecutive double hybridization of cDNA and rDNA-Fc for the sandwich assay for a) flat substrate and micropillar-structured ones with increasing pitch of b) 19 µm, c) 14 µm, d) 10 µm and e) 8 µm size. Freshly prepared 0.1 M $NaClO_4$ solution was degassed for 5 min and used as electrolyte for the all CV experiments. All the solutions were prepared in PBS (pH 7.4) at concentration of 1 mg/ml and 1 µM, respectively for PLL-OEG-DBCO and PNA, while 0.5 µM for both cDNA and rDNA-Fc in the same buffer.

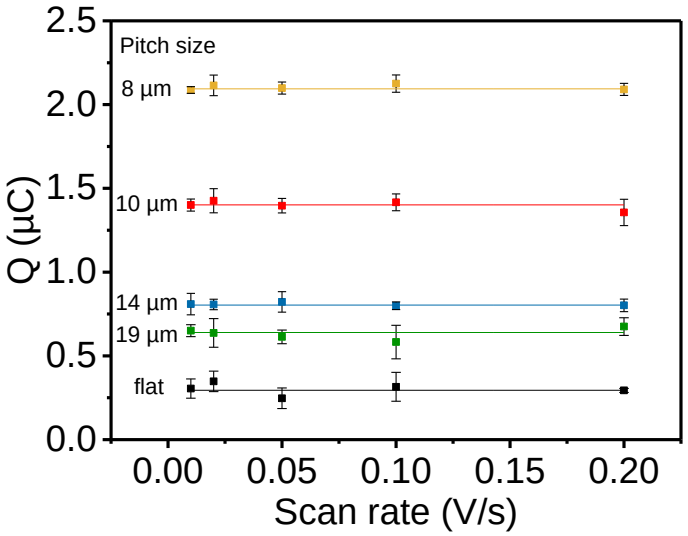

Figure S11. Dependence of the amount of charges involved in the redox process (Q) versus scan rate (0.01 – 0.2 V/s), derived from the average values from experiments in Figure S10. The substrates used were flat (black), 19 µm (green), 14 µm (blue), 10 µm (red) and 8 µm (ochre) pitch. Prior to the CV experiments, freshly prepared 0.1 M $NaClO_4$ solution was degassed for 5 min and used as the electrolyte. The concentrations of PLL-OEG-DBCO and PNA were 1.0 mg/ml and 0.5 µM respectively, while 1 µM for both cDNA and rDNA-Fc in PBS (7.4). Datapoints corresponds to two measurements.

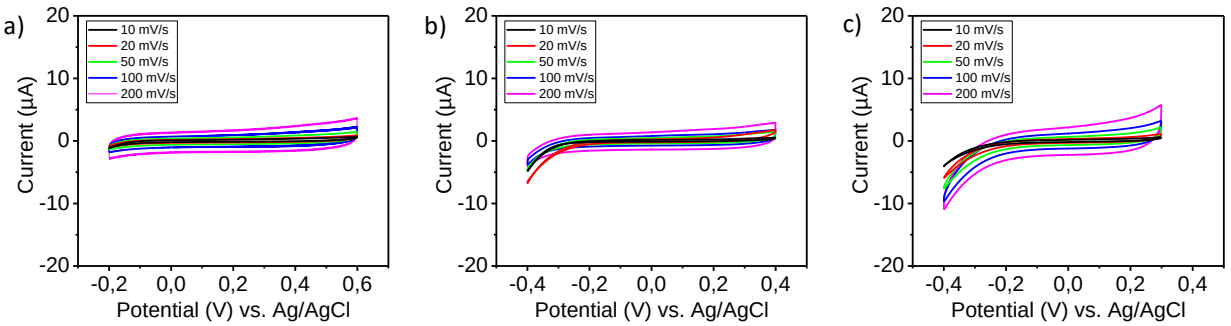

Figure S12. Voltammograms of the control experiments at gold flat surface functionalized with PLL-OEG(27.6)-DBCO(3.0). a) Selectivity experiment performed after the immobilization of PNA-azide and using ncDNA in the sandwich assay. Evaluation of the specific electrochemical response of the biosensing layer and the sandwich assay when b) the PNA probe anchoring or c) the cDNA hybridization step are missing. Before each CV experiments, freshly prepared 0.1 M $NaClO_4$ electrolyte solution was degassed for 5 min. The concentrations of the components used were 1.0 mg/ml for modified PLL, 0.5 µM for PNA-azide, cDNA and rDNA-Fc. All the deposition steps were done in PBS (pH 7.4).

Quantification of the area under the reduction peak at cyclic voltammograms

To obtain the points of the amount of charges involved in the redox process (Q) in Figure S11, the cyclic voltammograms in Figure S10 were treated according to the following procedure: the first derivative was applied to the anodic segment of interest to find the peak potential (E_p). A range of ± 0.25 V was defined from the E_p to set the baseline between these potentials and the peak area, related to (Q), was recorded. All the passages were performed by means of the CHI760D software (CH Instruments, Inc. Austin, USA).

Probe density determination by CV

The average surface coverage of rDNA-Fc molecules for the flat and micropillar-structured substrates was calculated adapting the following equation:[7]

$$\Gamma = Q/nFA \qquad \text{eq. 7}$$

where Γ is the surface coverage (mol/cm^2), Q is the area of the reductive signal (in C), F is the Faraday constant (96485.34 C/mol), n is the number of electrons involved in the redox process (1 for ferrocene), and A the total active surface area of the working electrode. To show the effect of the pitch variation, eq. 8 was derived to obtain calculated values of Q, Q_{calc}, to obtain the dependence of Q on the pitch:

$$Q_{calc} = nF\Gamma(SE_pPA_p + SE_fPA_f) \qquad \text{eq. 8}$$

Here, SE_p is dependent on p as described above (eq. 4), and the second term is a constant which is shown as the abscissa. Γ is thus obtained from the slope of the fitting in Figure 5. Results expressed in molecules/cm^2 have been calculated by multiplying Γ by the Avogadro's number (N_A).

References

(1) Veerbeek, J.; Steen, R.; Vijselaar, W.; Rurup, W. F.; Korom, S.; Rozzi, A.; Corradini, R.; Segerink, L.; Huskens, J. Selective Functionalization with PNA of Silicon Nanowires on Silicon Oxide Substrates. *Langmuir* **2018**, *34*, 11395–11404.

(2) Bettegowda, C.; Sausen, M.; Leary, R. J.; Kinde, I.; Wang, Y.; Agrawal, N.; Bartlett, B. R.; Wang, H.; Luber, B.; Alani, R. M.; Antonarakis, E. S.; Azad, N. S.; Bardelli, A.; Brem, H.; Cameron, J. L.; Lee, C. C.; Fecher, L. A.; Gallia, G. L.; Gibbs, P.; Le, D.; Giuntoli, R. L.; Goggins, M.; Hogarty, M. D.; Holdhoff, M.; Hong, S.-M.; Jiao, Y.; Juhl, H. H.; Kim, J. J.; Siravegna, G.; Laheru, D. A.; Lauricella, C.; Lim, M.; Lipson, E. J.; Marie, S. K. N.; Netto, G. J.; Oliner, K. S.; Olivi, A.; Olsson, L.; Riggins, G. J.; Sartore-Bianchi, A.; Schmidt, K.; Shih, L.-M.; Oba-Shinjo, S. M.; Siena, S.; Theodorescu, D.; Tie, J.; Harkins, T. T.; Veronese, S.; Wang, T.-L.; Weingart, J. D.; Wolfgang, C. L.; Wood, L. D.; Xing, D.; Hruban, R. H.; Wu, J.; Allen, P. J.; Schmidt, C. M.; Choti, M. A.; Velculescu, V. E.; Kinzler, K. W.; Vogelstein, B.; Papadopoulos, N.; Diaz, L. Detection of Circulating Tumor DNA in Early- and Late-Stage Human Malignancies. *Sci. Transl. Med.* **2014**, *6*, 1–11.

(3) Thierry, A.; Mouliere, F.; El Messaoudi, S.; Mollevi, C.; Lopez-Crapex, E.; Rolet, F.; Gillet, B.; Gongora, C.; Dechelotte, P.; Robert, B.; Del Rio, M.; Lamy, P.; Bibeau, F.; Nouaille, M.; Loriot, V.; Jarrousse, A.; Molina, F.; Mathonnet, M.; Pezet, D.; Ychou, M. Clinical Validation of the Detection of KRAS and BRAF Mutations from Circulating Tumor DNA. *Nat. Med.* **2014**, *20*, 430–435.

(4) Movilli, J.; Rozzi, A.; Ricciardi, R.; Corradini, R.; Huskens, J. Control of Probe Density at DNA Biosensor Surfaces Using Poly(L-Lysine) with Appended Reactive Groups. *Bioconjug. Chem.* **2018**, *29*, 4110–4118.

(5) Di Iorio, D.; Marti, A.; Koeman, S.; Huskens, J. Clickable Poly-L-Lysine for the Formation of Biorecognition Surfaces. RSC Adv. 2019, 9, 35608–35613.

(6) Schröper, F.; Brüggemann, D.; Mourzina, Y.; Wolfrum, B.; Offenhäusser, A.; Mayer, D. Analyzing the Electroactive Surface of Gold Nanopillars by Electrochemical Methods for Electrode Miniaturization. *Electrochim. Acta* **2008**, *53*, 6265–6272.

(7) Pheeney, C. G.; Barton, J. K. DNA Electrochemistry with Tethered Methylene Blue. *Langmuir* **2012**, *28*, 7063–7070.